



# Connecting microstructural coarsening processes to electrochemical performance in solid oxide fuel cells: An integrated modeling approach



Fadi Abdeljawad<sup>a</sup>, Benjamin Völker<sup>b</sup>, Ryan Davis<sup>a</sup>, Robert M. McMeeking<sup>b</sup>,  
Mikko Haataja<sup>a,c,d,\*</sup>

<sup>a</sup> Department of Mechanical and Aerospace Engineering, Princeton University, Princeton, NJ 08544, USA

<sup>b</sup> Department of Mechanical Engineering, University of California at Santa Barbara, Santa Barbara, CA 93106, USA

<sup>c</sup> Princeton Institute for the Science and Technology of Materials (PRISM), Princeton University, Princeton, NJ 08544, USA

<sup>d</sup> Program in Applied and Computational Mathematics (PACM), Princeton University, Princeton, NJ 08544, USA

## HIGHLIGHTS

- Integrated model: a phase-field model and an electrochemical cell one are linked.
- Using the integrated model, we study the role of Ni coarsening on SOFC performance.
- Simple scaling laws describe the evolution of key microstructural features.
- Ni particle size strongly affects morphological evolution in Ni–YSZ SOFC anodes.
- Integrated approach facilitates identification of parameters associated with stable microstructures and/or optimal performance.

## ARTICLE INFO

### Article history:

Received 6 May 2013

Received in revised form

24 October 2013

Accepted 25 October 2013

Available online 5 November 2013

### Keywords:

Topological evolution

Microstructure

Solid oxide fuel cell (SOFC)

Ni coarsening

Phase field

Electrochemical performance

## ABSTRACT

In solid oxide fuel cells (SOFCs), Ni coarsening in porous anodes that are comprised of Ni and yttria stabilized zirconia (YSZ) leads to changes in several microstructural attributes, which affect the electrochemical performance. Herein we present an integrated modeling approach, where a dynamic mesoscale phase field model is linked with a stationary macroscale electrochemical cell level model in order to assess the role of Ni coarsening on the performance of SOFCs. The phase field model is capable of capturing the morphological evolution of Ni and accounting for its polycrystalline nature, while the electrochemical model encompasses the entire set of processes of gas transport, electronic and ionic conduction as well as the electrochemical reactions. Microstructural features are extracted from the phase field model as anode systems evolve over time and employed as effective properties in the electrochemical model. Simulation results highlight the importance of Ni and YSZ particle size and ratio on both the microstructural stability and electrochemical performance of SOFCs. In particular, it is shown that, for the classes of microstructures employed in this work, coarsening of Ni particles can either improve or diminish the maximum power density relative to the as-sintered ones, depending on the initial particle size.

© 2013 Elsevier B.V. All rights reserved.

## 1. Introduction

Solid oxide fuel cells (SOFCs) are regarded as alternative devices for cleaner and more efficient energy conversion [1–3]. With the advantages of high efficiency of 60%–80% [4,5] and reduced carbon emissions [6], SOFCs are being developed for various stationary and auxiliary commercial power applications with a desired lifetime of 40,000 h or more [7]. In conventional SOFCs, which operate at temperatures in the range 800–950 °C [8,9], a thin film of yttria-stabilized zirconia (YSZ) is utilized as the oxygen ion conducting

\* Corresponding author. Department of Mechanical and Aerospace Engineering, Princeton University, Princeton, NJ 08544, USA. Tel.: +1 609 2589126; fax: +1 609 2585877.

E-mail addresses: [fabdelja@princeton.edu](mailto:fabdelja@princeton.edu) (F. Abdeljawad), [benvoelker@gmail.com](mailto:benvoelker@gmail.com) (B. Völker), [rsdavis@princeton.edu](mailto:rsdavis@princeton.edu) (R. Davis), [rmcm@engineering.ucsb.edu](mailto:rmcm@engineering.ucsb.edu) (R.M. McMeeking), [mhaataja@princeton.edu](mailto:mhaataja@princeton.edu) (M. Haataja).

ceramic membrane. A porous composite of lanthanum strontium manganate (LSM) and YSZ is typically used for the cathode and a state-of-the-art anode is a porous Ni–YSZ composite [10].

In SOFCs, oxygen is electrochemically reduced at the cathode, from which the oxygen ions subsequently diffuse through the electrolyte and react with the oxidized fuel at the anode. The anode in turn is a porous, complex three phase material, within which all phases (pore, conducting metal, and ceramic oxide) percolate. The contiguity of the pore phase ensures effective transport of the fuel to the catalytic sites, while contiguous metallic and ceramic oxide phases serve as conduits of the charges (electrons and oxygen ions) involved in the electrochemical reactions taking place in the vicinity of three-phase boundaries (TPBs), which constitute the electrochemically active regions [11]. The anode must maintain a stable microstructure over extended periods of time at elevated temperatures, as well as high electron and ion conductivity and catalytic activity.

Electrochemical performance degradation in SOFC cermet anodes is usually attributed to several phenomena and processes at the microstructural level, such as poisoning by fuel impurities, coking, thermal and redox cycling [11–16], as well as microstructural coarsening processes associated with Ni particles in Ni-based cermet anodes [9,17,18]. Coarsening is a competitive growth process, which leads to a reduction in the total interfacial energy. Spatial variations in the mean interface curvature induce diffusional fluxes, which transfer material from regions of high mean curvature to ones associated with lower mean curvature. In the case of isotropic interfacial energies, coarsening leads to a reduction in the total interfacial area [19,20].

Indeed, Ni coarsening in SOFC anodes has been the subject of several experimental investigations in recent years [11,21–24]. These studies have revealed that performance degradation can be directly linked to changes in several microstructural features associated with coarsening processes, such as extent of TPBs, total interfacial areas, and contiguity of anode phases. In particular, the density of TPB lines, which is often employed as a simple metric to predict electrochemical performance, is found to decrease due to Ni coarsening [23]. Simwonis et al. [21] studied Ni–YSZ composite anodes under operating environments and observed a decrease in the electrical conductivity due to Ni coarsening. Moreover, Ni phase coarsening is found to affect phase contiguity [25]. A recent study by Cronin et al. [26] revealed that Ni coarsening affects several microstructural attributes, such as pore percolation, and total pore and Ni-pore interfacial areas.

While the aforementioned experimental studies have provided important insights to the evolution of anode microstructures in operating environments, they do not examine the effects of inter-related physical phenomena on coarsening rates. Computational models on the other hand are ideally suited for exploring the various hypothesized mechanisms that control microstructural evolution processes in SOFC anodes. Existing computational studies of Ni coarsening in SOFC anodes include two-particle systems [27], phase field models [28,29], and multi-scale frameworks [30]. Our approach builds on and significantly extends these previous computational studies by incorporating the coupling between microstructural evolution and electrochemical performance while accounting for the polycrystalline nature of the Ni phase.

In this work, we focus, in a parametric study, on the role of anode microstructure, characterized by Ni particle size and Ni to YSZ particle size ratio, on the topological evolution of SOFC anodes and its impact on electrochemical performance. More specifically, we present an integrated modeling approach to examine the impact of Ni phase coarsening in Ni–YSZ porous anodes on the performance of SOFC cells. In this approach, several representative anode microstructures with tunable features (such as phase

volume fractions and particle sizes) are first generated “virtually”. Next, a mesoscale diffuse-interface model, which is capable of capturing Ni–YSZ interaction, and accounting for the polycrystalline nature of Ni, is employed to quantitatively investigate the coarsening of Ni phase particles in said microstructures. Then, morphological features are extracted from the phase field model as the anode systems evolve over time and employed as effective input parameters to a recently developed macroscale cell level model to quantitatively evaluate the time-dependent electrochemical performance [31]. Here, we note that while the electrochemical model itself is time-independent, its input parameters, which represent effective properties that depend on the anode microstructure, are evolving in time and tracked via the phase field model.

Starting from a binary mixture of numerically sintered Ni and YSZ particles, our simulation results conclusively demonstrate that the overall TPB length decreases monotonically during coarsening. Furthermore, the reduction in the overall TPB length obeys a simple scaling law in time. In addition, the contiguity of the Ni phase, which also monotonically decreases during coarsening, displays an interesting size effect, such that systems with initially small Ni particles lose contiguity faster. Finally, the overall electrochemical performance can display a non-monotonic time-dependence during coarsening, and even improve over time. For initially coarse microstructures, the electrochemical performance is dominated by the electrochemical reactions taking place in the vicinity of TPBs, the length of which decreases monotonically. For initially fine microstructures, on the other hand, electrochemical performance is dominated by gaseous transport processes through the pore phase, leading to an increase in the maximum power density over time as the average pore size increases due to coarsening.

More broadly speaking, simulation results highlight the importance of initial anode microstructure on the stability and performance of SOFC anodes. Our modeling approach can be used as a design tool to identify combinations of morphological parameters, such as Ni and YSZ particle size and ratio that yield porous anode systems with optimal microstructural stability and electrochemical performance characteristics.

The rest of the manuscript is organized as follows. In Section 2 we first outline both the continuum modeling framework and the cell level approach to evaluate the electrochemical performance based on microstructural parameters. Then, in Section 3 we describe how the initial microstructures are generated and characterized. Quantitative results from coarsening studies and their

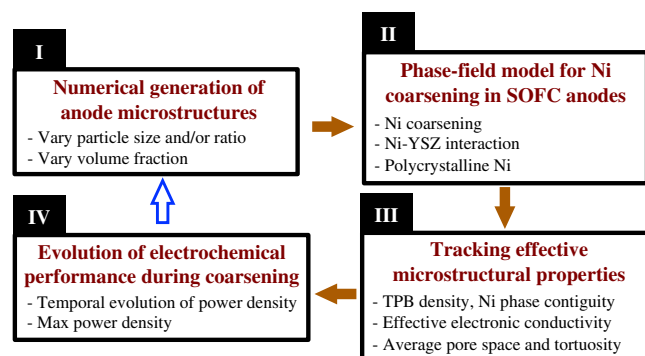


**Fig. 1.** A block diagram illustrating the integrated modeling approach that is used to examine the role of Ni coarsening in Ni–YSZ porous anodes on the electrochemical performance of SOFCs. The arrow outlined in blue represents the feedback from the electrochemical model to the input microstructures, which in turn closes the design iteration loop. This step is not implemented in the work presented here. (For interpretation of the references to color in this figure legend, the reader is referred to the web version of this article.)

implications to electrochemical performance are in turn discussed in Section 4. Finally, concluding remarks are presented in Section 5.

## 2. An integrated modeling approach

Our computational approach links a mesoscale phase field model for Ni coarsening in Ni–YSZ porous anodes to a macroscale cell level model, which evaluates the electrochemical performance of SOFCs. The aforementioned models are implemented as follows. First, the phase field model is used to track the evolution of several microstructural features as “virtual” anode systems evolve over time. Next, these features are extracted from the phase field model and used as inputs to the cell level model in order to evaluate the electrochemical performance of these systems. A block diagram illustrating our modeling approach is shown in Fig. 1.

Below, we first describe the salient features of the phase field formalism employed in our coarsening studies. Then, an overview of the cell level approach to predict the electrochemical performance, for a given microstructure, is provided. Finally, the numerical generation and microstructure characterization of “virtual” anode systems are described.

### 2.1. The phase field formalism

The challenge in microstructural evolution studies resides in accurately capturing the complex topological changes (such as merging of two or more particles or the disappearance of one) that take place during the coarsening process. The so-called phase field approach, which has already been employed in studies of SOFC microstructures by other groups [28–30], elegantly incorporates such topological changes in a numerically convenient manner as discussed next.

The starting point of our phase-field model is the introduction of order parameters for the phases in porous Ni–YSZ anodes. Additional structural order parameters are also introduced to represent the polycrystalline nature of the Ni phase and account for interfacial energies associated with Ni grain boundaries (GBs). Next, a total free energy  $\mathcal{F}_{\text{tot}}$  that describes the state of the anode system is constructed in terms of the order parameters and the dynamics of the system follow from the minimization of  $\mathcal{F}_{\text{tot}}$ . Consistent with experimental observations [22,26], a static, or non-evolving, order parameter  $\theta(\mathbf{x})$  is assigned to the YSZ phase, reflecting its microstructural stability. In contrast, the evolution of the Ni phase is tracked with the aid of an order parameter  $c(\mathbf{x},t)$  in combination with structural order parameters  $\{\eta_i(\mathbf{x},t), i = 1, \dots, n_\eta\}$  that describe the shape and crystallographic orientation of the Ni grains. Here,  $n_\eta$  is the number of structural order parameters needed to resolve the texture of the Ni phase. The order parameters are chosen such that (a) in the YSZ phase  $(\theta, c) = (1, -1)$ , (b) in the Ni phase  $(\theta, c) = (0, +1)$ , and (c) in the pore space  $(\theta, c) = (0, -1)$ . Furthermore,  $\theta(\mathbf{x}) \in (0, 1)$  and  $c(\mathbf{x},t) \in (-1, 1)$  define YSZ and Ni interfaces, respectively. For the structural order parameters, the equilibrium values are chosen such that within non-Ni phases (YSZ and pore):  $\{\eta_i = 0, i = 1, \dots, n_\eta\}$  and within a Ni grain  $\{\eta_i = 1, \eta_{j \neq i} = 0, i, j = 1, \dots, n_\eta\}$ . As is shown in Fig. 2, order parameters take on a constant value within the bulk phases and vary rapidly-but-smoothly across interfaces.

As in standard Ginzburg–Landau formalism and motivated by the work of Wang [32] on solid-state sintering, the following total chemical free energy is employed for an SOFC anode system:

$$\mathcal{F}_{\text{tot}}[c, \theta, \{\eta_i\}] = \int d\mathbf{x} \left[ f_{\text{bulk}} + \frac{w^2}{2} |\nabla c|^2 + \sum_{i=1}^{n_\eta} \frac{k_i^2}{2} |\nabla \eta_i|^2 + f_{\text{wett}} \right], \quad (1)$$

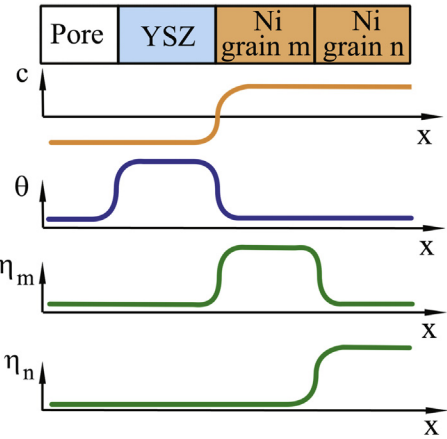


Fig. 2. A schematic illustrating the order parameters used in the phase field model.  $\theta$  and  $c$  parameters are for the YSZ and Ni phases, respectively.  $\eta_m$  and  $\eta_n$  are structural order parameters for Ni grains  $m$  and  $n$ , respectively.

where  $w$  and  $k_i$  are so-called gradient energy coefficients employed to tune the Ni surface and grain boundary energies. The first term on the right hand side ( $f_{\text{bulk}}$ ) is a fourth-order Landau polynomial that defines the homogeneous bulk free energy associated with the Ni phase and multiple Ni grains. In particular,  $f_{\text{bulk}}$  is constructed such that the equilibrium values for the order parameters, i.e.  $\partial f_{\text{bulk}} / \partial c = \partial f_{\text{bulk}} / \partial \eta_i = 0$ , are  $(c = -1, \eta_i = 0, i = 1, \dots, n_\eta)$  within non-Ni phases and  $(c = +1, \eta_i = +1, \eta_{j \neq i} = 0, i, j = 1, \dots, n_\eta)$  within a Ni grain. A convenient form for  $f_{\text{bulk}}$  that satisfies these requirements is

$$f_{\text{bulk}}(c, \{\eta_i\}) = m_H (c^2 - 1)^2 + A_H \left\{ \frac{1}{4} (c + 1)^2 + 3(1 - c) \sum_{i=1}^{n_\eta} \eta_i^2 - 2(3 - c) \sum_{i=1}^{n_\eta} \eta_i^3 + 3 \left[ \sum_{i=1}^{n_\eta} \eta_i^2 \right]^2 \right\}, \quad (2)$$

where  $m_H$  and  $A_H$  are parameters we employ to tune the interfacial energies and interface widths. In this work, it is assumed that GB interfaces are isotropic, yielding  $k_i = k$ . The last term ( $f_{\text{wett}}$ ) on the right hand side of Eq. (1) accounts for the interaction between the Ni and YSZ phases, and the resulting wetting angle at triple junctions. In this work,  $f_{\text{wett}}$  is written as

$$f_{\text{wett}}(c, \theta) = -\xi_1 c |\nabla \theta|^2 + \xi_2 \theta (c - c^3/3), \quad (3)$$

where  $\xi_1$  and  $\xi_2$  are model parameters employed to tune the equilibrium Ni–YSZ wetting angle, experimentally observed to be  $\geq 117^\circ$  [33].

With the proposed total chemical free energy functional in Eq. (1) and following the treatment of Cahn and Hilliard [34], the interfacial energies and widths can be evaluated analytically. In particular, we obtain the Ni surface energy  $\gamma_s \approx 4w\sqrt{2m_H/3} + k\sqrt{A_H/3}$  and interfacial width  $\delta_s \sim 2w/\sqrt{2m_H}$ , while Ni GB energy  $\gamma_{\text{GB}} \approx 2k\sqrt{A_H/3}$  and its width  $\delta_{\text{GB}} \sim k/\sqrt{A_H}$ . Therefore, the phase field model parameters  $w$ ,  $m_H$ ,  $A_H$  and  $k$  are uniquely determined from the Ni phase interfacial and GB energies and widths.

Within the Ginzburg–Landau formalism and with the aid of variational derivatives, the governing equations for the evolution of  $c(\mathbf{x},t)$  and  $\{\eta_i(\mathbf{x},t), i = 1, \dots, n_\eta\}$  for  $(\mathbf{x},t) \in V \times [0,T] \subset \mathbb{R}^3 \times \mathbb{R}$ , where  $V$  is the domain volume and  $T$  is the final time, can be stated respectively as

$$\frac{\partial c}{\partial t} = \nabla \cdot \left[ M \nabla \left( \frac{\delta \mathcal{F}_{\text{tot}}}{\delta c} \right) \right], \quad (4a)$$

$$\frac{\partial \eta_i}{\partial t} = -L_i \frac{\delta \mathcal{F}_{\text{tot}}}{\delta \eta_i}, \quad i = 1, 2, \dots, n_\eta, \quad (4b)$$

where  $M$  denotes the Ni phase mobility function and  $L_i$  is a kinetic parameter associated with Ni GB mobility, where under the isotropy assumption of GB interfaces,  $L_i = L$ . At SOFC operating temperatures, Ni bulk self diffusion  $\sim 10^{-16} \text{ m}^2 \text{ s}^{-1}$  [35], whereas Ni surface self diffusion  $D_{\text{Ni}} \sim 10^{-11} \text{ m}^2 \text{ s}^{-1}$  [36]. We also note that the  $\text{Zr}^{4+}$  surface diffusion coefficient in YSZ is  $\sim 10^{-18} \text{ m}^2 \text{ s}^{-1}$  [37], justifying the assumption that YSZ particles do not significantly evolve during Ni coarsening. Since Ni diffusivity along YSZ interfaces is not well characterized, it is assumed that the coarsening of Ni in Ni–YSZ cermet anodes is dominated by Ni surface diffusion along Ni–pore interfaces. In this work, Ni phase mobility has the general form  $M = M_{\text{Ni}} Q(c, \nabla c, \theta, \nabla \theta)$ , where  $M_{\text{Ni}}$  is the Ni phase atomic mobility, and the detailed form of the dimensionless function  $Q$  is given below in Eq. (7).

The spatio-temporal evolution equations for  $c(\mathbf{x}, t)$  and  $\eta_i(\mathbf{x}, t)$  are made non-dimensional by introducing non-dimensional spatial coordinates  $\tilde{x} = x/d_0$  and time  $\tilde{t} = t/\tau$ , where  $d_0$  and  $\tau$  denote the characteristic length (voxel edge length) and time scales, respectively. For convenience, we also introduce the non-dimensional quantities  $\tilde{w}^2 = m_{\text{H}}/(2E)$ ,  $\tilde{m}_{\text{H}} = m_{\text{H}} d_0^2/(\delta_s^2 E)$ ,  $\tilde{A}_{\text{H}} = A_{\text{H}} d_0^2/(\delta_s^2 E)$ ,  $\tilde{\xi}_1 = \xi_1/(E \delta_s^2)$ , and  $\tilde{\xi}_2 = \xi_2 d_0^2/(E \delta_s^2)$ , where  $E$  is a reference energy density. Ni mobility can be written as  $M_{\text{Ni}} = D_{\text{Ni}}/(\partial \mu/\partial c)_{c_{\text{eq}}} = D_{\text{Ni}}/(\partial^2 f_{\text{bulk}}/\partial c^2)_{c_{\text{eq}}}$ . Therefore, the characteristic time  $\tau$  can be expressed as

$$\tau = \frac{m_{\text{H}} d_0^4 (\partial^2 f_{\text{bulk}}/\partial c^2)_{c_{\text{eq}}}}{E D_{\text{Ni}} \delta_s^2} \approx \frac{16 \tilde{w}^2 d_0^4}{D_{\text{Ni}} \delta_s^2}. \quad (5)$$

For the systems we examine in this work, where  $d_0 \sim 60 \text{ nm}$ ,  $\delta_s \sim 1 \text{ nm}$ , and  $D_{\text{Ni}} \sim 10^{-11} \text{ m}^2 \text{ s}^{-1}$ , the resulting characteristic time  $\tau \sim 40 \text{ s}$ . As for the governing equations for the non-conserved parameters, we introduce the non-dimensional  $\tilde{L} = \tau L E \delta_{\text{GB}}^2/d_0^2$  and  $\tilde{k}^2 = k^2/(E \delta_{\text{GB}}^2)$ . GB mobility  $M_{\text{GB}}$  and energy  $\gamma_{\text{GB}}$  are related to the model parameters through

$$L k^2 = M_{\text{GB}} \gamma_{\text{GB}} = \frac{\tilde{L} \tilde{k}^2 d_0^2}{\tau} \approx \frac{\tilde{L} \tilde{k}^2 D_{\text{Ni}} \delta_s^2}{16 \tilde{w}^2 d_0^2}, \quad (6)$$

where Eq. (5) has been employed in the last step.

The resulting non-dimensional spatio-temporal evolution equations for  $c(\mathbf{x}, t)$  and  $\eta_i(\mathbf{x}, t)$  have the same form as the original ones. For the remainder of this paper, we drop the tildes on all parameters for notational convenience. Finally, the form that is used for the Ni phase mobility

$$M = M_{\text{Ni}} \left[ \left( 1.0 - \tanh(|\nabla \theta|^2/h_1) \right) \tanh(|\nabla \hat{c}|^2/h_2) + M^* \tanh(|\nabla \theta|^2/h_1) \right], \quad (7)$$

where  $\hat{c} = \tanh(c/h_3)$ . The model parameters  $h_1$ ,  $h_2$  and  $h_3$  are employed to tune the range of  $c$  and  $\theta$  values that contribute to the mobility function, while  $M^*$  defines a mobility contribution for Ni diffusing along YSZ–pore interfaces. In this work, it is assumed that diffusion along Ni–pore interfaces is the dominant mass transport mechanism.

## 2.2. A cell level model for the electrochemical performance of SOFC systems

Due to the coarsening of the Ni phase, the microstructure in the reactive anode layer evolves with time. In order to systematically capture the effects of these microstructural changes on the electrochemical performance of the SOFC system, we employ a numerical cell level model encompassing the entire set of processes of gas transport, electronic and ionic conduction as well as the electrochemical reactions. For completeness, a brief overview of the approach is provided next; the reader is referred to Ref. [31] for a more detailed exposition of the framework.

The model geometry consists of a porous anode support and reactive layer, a dense electrolyte layer, and porous cathode reactive and current collector layers as illustrated in Fig. 3. In this work, we only consider the effects of the temporal microstructural changes associated with Ni coarsening in the reactive anode interlayer, while the effective properties of all other layers, i.e., anode support, dense electrolyte and cathode remain constant over time.

In our approach, we extract representative 3D anode microstructures from the phase-field model at regular time intervals, and compute the effective microstructural parameters that characterize the electrochemical performance of the reactive anode layer. These effective properties are then transferred into the stationary one-dimensional cell level model and serve as input parameters for computing the electrochemical performance. This approach yields temporal snapshots of the electrochemical performance, which enables us to quantitatively examine the role Ni phase coarsening on the evolution of electrochemical performance of SOFCs.

Now, the equations for mass transport and migration of electrons and oxygen ions in the reactive anode layer take the form of Poisson equations:

$$\nabla N_\alpha(R_{\text{pore}}, \alpha_\infty) = \frac{\Lambda_{\text{react}} i_{\text{an}}}{2F}, \quad (8)$$

$$\nabla \left( -\sigma_{\text{Ni}}^{\text{eff}} \nabla \Phi_{\text{Ni}} \right) = \Lambda_{\text{react}} i_{\text{an}}, \quad (9)$$

$$\nabla \left( -\sigma_{\text{YSZ}}^{\text{eff}} \nabla \Phi_{\text{YSZ}} \right) = -\Lambda_{\text{react}} i_{\text{an}}, \quad (10)$$

where  $N_\alpha$  denotes the rate of mass transport for gas species  $\alpha$  and is a function of the average pore radius,  $R_{\text{pore}}$ , and the pore tortuosity factor,  $\alpha_\infty$ . Further,  $\Lambda_{\text{react}}$  is the reactive TPB length,  $i_{\text{an}}$  the local Faradaic current density, and  $F$  the Faradaic constant. The diffusive gas transport is modeled using the dusty-gas approach [38], which accounts for both molecular and Knudsen diffusion, and detailed expressions used for  $N_\alpha(R_{\text{pore}}, \alpha_\infty)$  can be found in Ref. [31]. Ohm's law describes the transport of electrons and ions, where  $\sigma_{\text{Ni}}^{\text{eff}}$  is the effective electronic conductivity of the Ni phase,  $\sigma_{\text{YSZ}}^{\text{eff}}$  the effective

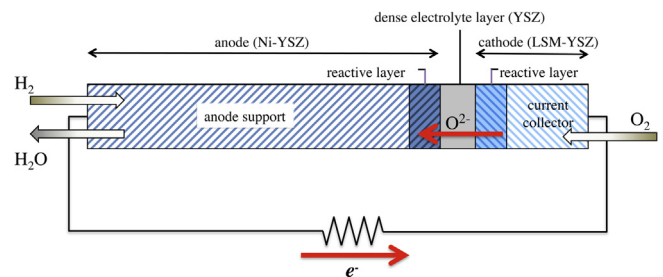


Fig. 3. A schematic illustration of an anode supported SOFC cell that is used for the analysis in this work.



**Table 1**

Parameters used in the 1D cell model for the functional layers: anode support (AS), reactive anode interlayer (AN), reactive cathode interlayer (CA) and cathode current collector (CC). Note that effective properties of the reactive anode interlayer that evolve due to Ni coarsening are designated “evolving” in this table.

Parameter	AS	AN	CA	CC	Ref.
$L$ [ $\mu\text{m}$ ]	1000	20	20	50	[39,56]
$p_0$ [Pa]	101,300	101,300	101,300	101,300	[17]
$(\phi_{\text{Ni}}, \phi_{\text{YSZ}})$	(0.26, 0.26)	(0.30, 0.45)	(0.38, 0.38)	(0.55, 0.0)	[39]
$\phi_{\text{pore}}$	0.48	0.25	0.24	0.45	[39]
$R_{\text{YSZ}}$ [ $\mu\text{m}$ ]	1.0		0.5	1.0	
$(R_{\text{Ni}}, R_{\text{pore}})$ [ $\mu\text{m}$ ]	(1.0, 1.62)	Evolving	(0.5, 0.29)	(1.0, 1.45)	[39,56]
$\Delta_{\text{react}}$ [ $\text{mm}^{-3}$ ]		Evolving	$5.72 \times 10^{12}$		
$\alpha_{\infty}$	1.65	Evolving	2.2	1.71	
$\sigma_{\text{Ni}}^{\text{eff}}$	0.033	Evolving	0.059	0.214	
$\sigma_{\text{YSZ}}^{\text{eff}}$		0.059	0.059		
$\beta_f, \beta_r$	0.5	0.5	0.5	0.5	[57]
$M_{\text{H}_2}$ [ $\text{mol}^{-1} \text{kg}$ ]	$2.016 \times 10^{-3}$	$2.016 \times 10^{-3}$			
$M_{\text{H}_2\text{O}}$ [ $\text{mol}^{-1} \text{kg}$ ]	$18.02 \times 10^{-3}$	$18.02 \times 10^{-3}$			
$M_{\text{O}_2}$ [ $\text{mol}^{-1} \text{kg}$ ]			$32.00 \times 10^{-3}$	$32.00 \times 10^{-3}$	
$M_{\text{N}_2}$ [ $\text{mol}^{-1} \text{kg}$ ]			$28.01 \times 10^{-3}$	$28.01 \times 10^{-3}$	
$(\xi_{\text{H}_2}, \xi_{\text{H}_2\text{O}})$ [K]	(59.7, 809.1)	(59.7, 809.1)			[58,59]
$(\xi_{\text{O}_2}, \xi_{\text{N}_2})$ [K]			(106.7, 71.4)	(106.7, 71.4)	[58,59]
$(\Gamma_{\text{H}_2}, \Gamma_{\text{H}_2\text{O}})$ [A]	(2.827, 2.641)	(2.827, 2.641)			[58,59]
$(\Gamma_{\text{O}_2}, \Gamma_{\text{N}_2})$ [A]			(3.467, 3.798)	(3.467, 3.798)	[58,59]
$E_{\text{H}_2}$ [J $\text{mol}^{-1}$ ]	$120 \times 10^3$	$120 \times 10^3$			[60]
$E_{\text{O}_2}$ [J $\text{mol}^{-1}$ ]			$130 \times 10^3$	$130 \times 10^3$	[60]
$G_{\text{H}_2}$ [J $\text{mol}^{-1}$ ]	$-147.1 \times 10^3$	$-147.1 \times 10^3$			[61]
$G_{\text{H}_2\text{O}}$ [J $\text{mol}^{-1}$ ]	$-454.9 \times 10^3$	$-454.9 \times 10^3$			[61]
$G_{\text{O}_2}$ [J $\text{mol}^{-1}$ ]			$-228.0 \times 10^3$	$-228.0 \times 10^3$	[61]
$G_{\text{O}^{2-}}$ [J $\text{mol}^{-1}$ ]	$-236.4 \times 10^3$	$-236.4 \times 10^3$	$-236.4 \times 10^3$	$-236.4 \times 10^3$	[61]

ionic conductivity of the YSZ phase,  $\Phi_{\text{Ni}}$  the electric potential in the Ni phase and  $\Phi_{\text{YSZ}}$  the ionic potential in the YSZ phase. The charge transfer rate correlated with the hydrogen oxidation reaction taking place in the reactive anode layer is described by a Butler–Volmer equation as

$$i_{\text{an}} = i_{\text{an}}^0(\Gamma_{\text{an}}) \left[ \exp\left(\beta_f \frac{2F}{RT} \zeta_{\text{an}}\right) - \exp\left(-\beta_r \frac{2F}{RT} \zeta_{\text{an}}\right) \right], \quad (11)$$

where  $\beta_f$  and  $\beta_r$  are the forward and reverse charge transfer coefficients,  $R$  is the universal gas constant,  $T$  is the temperature and  $\zeta_{\text{an}}$  is the anodic overpotential. For a detailed expression of the anodic reference exchange current density,  $i_{\text{an}}^0(\Gamma_{\text{an}})$ , where the parameter  $\Gamma_{\text{an}}$  is a fitting constant in our model, the reader is referred to Ref. [31]. Likewise, we describe all physical processes of gas transport, electron and ion migration and electrochemical redox reactions in the remaining layers: electron transport and diffusion of hydrogen and water vapor in the anode support layer, oxygen ion transport through the dense electrolyte layer, the oxygen reduction reaction and ion transport in the reactive cathode layer as well as the transport of electrons and the diffusion of oxygen and nitrogen (atmospheric air) through the cathode current collector and reactive cathode layer.

Our model [31] is parameterized based on experimental results reported by Zhao and Virkar [39], who consider a laboratory anode-supported SOFC button cell. Their cell is operating at a constant

temperature of  $T_{\text{ref}} = 1073$  K with hydrogen and  $\text{H}_2\text{O}$  vapor partial pressures at the anode support inlet of  $p_{\text{H}_2} = 0.97p_{0,\text{an}}$  and  $p_{\text{H}_2\text{O}} = p_{0,\text{an}} - p_{\text{H}_2}$ , and oxygen and nitrogen partial pressures at the cathode current collector inlet of  $p_{\text{O}_2} = 0.21p_{0,\text{ca}}$  and  $p_{\text{N}_2} = p_{0,\text{ca}} - p_{\text{O}_2}$  (atmospheric air) at a uniform total gas pressure of  $p_{0,\text{an}} = p_{0,\text{ca}} = 101.3$  kPa. As schematically illustrated in Fig. 3, the cell consists of an anode support layer of dimensions  $L_{\text{as}} = 1000$   $\mu\text{m}$ , a reactive anode interlayer ( $L_{\text{an}} = 20$   $\mu\text{m}$ ), a dense electrolyte layer ( $L_{\text{yte}} = 8$   $\mu\text{m}$ ), a reactive cathode interlayer ( $L_{\text{ca}} = 20$   $\mu\text{m}$ ) and a current collector ( $L_{\text{cc}} = 50$   $\mu\text{m}$ ). These dimensions and the model parameters of all layers are chosen to correspond to the experimental values published by Zhao and Virkar [39], and summarized in Table 1. The bulk conductivities of Ni, YSZ and LSM at  $T_{\text{ref}} = 1073$  K are taken from the literature [40] as  $\sigma_{\text{Ni},0} = 3.03 \times 10^4 \Omega^{-1} \text{m}^{-1}$ ,  $\sigma_{\text{YSZ},0} = 2.26 \Omega^{-1} \text{m}^{-1}$  and  $\sigma_{\text{LSM},0} = 1.28 \times 10^4 \Omega^{-1} \text{m}^{-1}$ , and the fitting constants of the model are determined as  $\Gamma_{\text{an}} = 4 \times 10^{-4} \text{A m}^{-1}$  and  $\Gamma_{\text{ca}} = 3.75 \times 10^{-4} \text{A m}^{-1}$  by using a best-fitting approach. Assuming a steady state operating condition for the fuel cell, i.e., treating gas flow as well as electronic and ionic currents as time-independent, the model is numerically solved using the commercial finite-element software COMSOL Multiphysics 3.5a, with cell level boundary conditions as described in Ref. [31].

### 3. SOFC electrodes

#### 3.1. Numerical generation of SOFC electrode microstructures

Virtual random packing systems of spherical particles are utilized in the integrated modeling approach for the microstructural evolution of SOFC anodes and its impact on the electrochemical performance. SOFC electrodes (anode and cathode) are idealized as binary mixtures of electron and ion conducting particles. The influence of the local anode microstructure characterized by the Ni to YSZ particle size ratio on the coarsening of Ni and the subsequent electrochemical performance is investigated. Here it is assumed that cathode does not undergo any evolution processes that influence its microstructure.

**Table 2**

Properties of virtual SOFC anode systems considered in this study. The as-prepared anode active layer is idealized as a binary mixture of electron and ion conducting spherical particles with radii  $R_{\text{Ni}}$  and  $R_{\text{YSZ}}$ , respectively. For all cases, the volume fractions of Ni ( $\phi_{\text{Ni}}$ ), YSZ ( $\phi_{\text{YSZ}}$ ) and pore ( $\phi_{\text{pore}}$ ) phases are  $30 \pm 2\%$ ,  $45 \pm 2\%$ ,  $25 \pm 2\%$ , respectively.

System name	$R_{\text{Ni}}/R_{\text{YSZ}}$	Number of Ni particles	Number of YSZ particles
R1	1.00	60	90
R1.5	0.67	206	92
R2	0.50	503	95
R2.5	0.40	1010	97

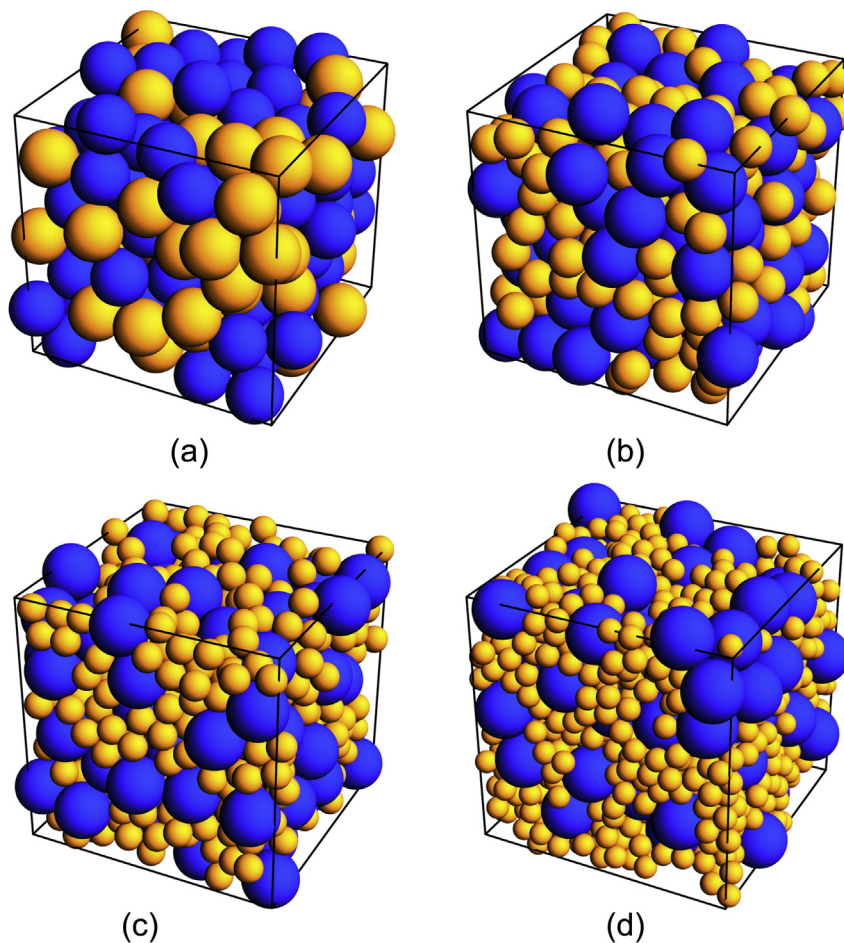


**Fig. 4.** Perspective views of the virtual, as-prepared anode microstructures. Ni and YSZ particles are represented in orange and blue, respectively. (a) R1 system:  $R_{\text{Ni}} = R_{\text{YSZ}}$  (b) R1.5 system:  $R_{\text{Ni}} = 0.67R_{\text{YSZ}}$  (c) R2 system:  $R_{\text{Ni}} = 0.5R_{\text{YSZ}}$  (d) R2.5 system:  $R_{\text{Ni}} = 0.4R_{\text{YSZ}}$ . In all systems, the volume fractions of Ni ( $\phi_{\text{Ni}}$ ), YSZ ( $\phi_{\text{YSZ}}$ ) and pore ( $\phi_{\text{pore}}$ ) are 30%, 45%, 25%, respectively, with  $\pm 2\%$  added to all fractions. Note that the YSZ particle size is fixed in all systems and only the number and size of Ni particles are varied. (For interpretation of the references to color in this figure legend, the reader is referred to the web version of this article.)

We use the random close packing algorithm of Gan et al. [41,42] to generate binary mixtures of spherical particles with periodic boundary conditions. Then, in order to numerically mimic the effect of sintering and enable the formation of connected particle clusters, overlap between the particles is generated by expanding the radii of all spheres uniformly and proportional to the radius while keeping the center of each sphere at a fixed position, until a desired densification is reached. Four virtual Ni–YSZ anodes are examined, denoted R1, R1.5, R2, R2.5, with Ni to YSZ particle radius ratio  $R_{\text{Ni}}/R_{\text{YSZ}} = 1.0, 0.67, 0.50$  and  $0.40$ , respectively. For all systems studied in this work, the resulting volume fractions of Ni ( $\phi_{\text{Ni}}$ ), YSZ ( $\phi_{\text{YSZ}}$ ) and pore ( $\phi_{\text{pore}}$ ) phases are  $30 \pm 2\%$ ,  $45 \pm 2\%$ ,  $25 \pm 2\%$ , respectively, similar to experimentally characterized Ni–YSZ based cermet anodes [22,23]. Furthermore, in this parametric study, the size of YSZ particles is kept constant. For a given SOFC anode system, or a given  $R_{\text{Ni}}/R_{\text{YSZ}}$  ratio, the size and number of Ni particles are varied in order to attain the target volume fraction. Table 2 lists the Ni to YSZ particle size ratio and the number of Ni and YSZ particles for each SOFC anode system used in this work. Perspective views of the R1, R1.5, R2 and R2.5 systems depicting Ni and YSZ particles and the resulting virtual anode microstructures are in turn shown in Fig. 4, where Ni and YSZ particles are colored in orange and blue, respectively. Finally, to account for sample-to-sample variations, coarsening simulations on four ensembles for each SOFC anode

system are performed and results are averaged for the use of the electrochemical performance analysis.

### 3.2. Microstructural characterization

Several microstructural attributes, whose evolution directly affects the electrochemical performance, are monitored during the course of Ni phase coarsening in the reactive anode layer. Of special interest are the effective material properties used in Eqs. (8–10) of the cell level model: the reactive TPB  $\Lambda_{\text{react}}$ , the average pore radius  $R_{\text{pore}}$ , and the pore tortuosity factor  $\alpha_{\infty}$ , as well as the effective conductivities  $\sigma_{\text{Ni}}^{\text{eff}}$  and  $\sigma_{\text{YSZ}}^{\text{eff}}$ . The fields  $c(\mathbf{x}, t)$  and  $\theta(\mathbf{x}, t)$  are extracted from the phase field model at several time steps during the temporal evolution of anode systems, and used to describe the topology of three-phase anodes.

#### 3.2.1. Percolation and three-phase boundary

We define the percolation degree  $P_D$  as the fraction of a phase that belongs to spatially contiguous clusters, i.e. percolating clusters that span the simulation box from end to end. For example,  $P_D = 0.5$  indicates that 50% of the Ni phase belongs to Ni clusters that are spatially contiguous. Spatially isolated clusters are identified using the labeling algorithm developed by Hoshen and Kopelman [43]. It is worth mentioning here that the YSZ phase in all

anode systems used in this study is a non-evolving one with a constant percolation degree  $\sim 99.5\%$ . Therefore, it is sufficient to only monitor the temporal evolution of the Ni phase percolation degree  $P_D$ .

Junctions in the microstructure of the porous anode, where the Ni, YSZ and pore phases meet define the three-phase boundary, where electrochemical reactions take place. We distinguish between the total TPB,  $\Lambda_{\text{tot}}$ , which accounts for all junctions where the three phases meet, and the reactive TPB,  $\Lambda_{\text{react}}$ , which only accounts for the fraction of junctions where the constituents of all three phases belong to percolated clusters. Using the percolation information we obtain during the evolution of SOFC anodes, we determine the length of the reactive TPB,  $\Lambda_{\text{react}}$ , by counting voxel edges where percolated Ni, YSZ and pore voxels meet. The length of reactive TPB,  $\Lambda_{\text{react}}$ , in porous SOFC electrodes represents an important parameter for the electrochemical performance as it dictates the overall charge transfer rate of the redox reactions.

### 3.2.2. Pore space properties

Serving as input parameters for modeling the diffusive gas transport through the pore network (cf. Eq. (8)), the average pore radius,  $R_{\text{pore}}$ , and the pore tortuosity factor,  $\alpha_\infty$ , are extracted from the voxel discretized electrode microstructures. In order to determine  $R_{\text{pore}}$ , we first define the pore phase field  $\Sigma(\mathbf{x}, t)$ , where  $\Sigma = 1$  denotes the pore phase and zero elsewhere. Then, we compute the two-point correlation function  $g_2(\mathbf{r}, t) = \langle [\Sigma(\mathbf{r}, t) - \langle \Sigma(\mathbf{r}, t) \rangle] [\Sigma(\mathbf{r}', t) - \langle \Sigma(\mathbf{r}', t) \rangle] \rangle / \mu$ , where  $\mu = \langle \Sigma^2(\mathbf{r}, t) \rangle - \langle \Sigma(\mathbf{r}, t) \rangle^2$  is the variance. The average pore radius  $R_{\text{pore}}$  is defined as the full width at half maximum of  $g_2(\mathbf{r}, t)$  [44].

When considering the diffusion of fuel gas through porous media, the irregular geometry of the pore space shows a significant effect: gas molecules are forced to follow tortuous pathways through the pore space, which slows down the rate of diffusional transport. In the dusty-gas model used, this effect is taken into account by the pore tortuosity factor,  $\alpha_\infty$ . A Lattice-Monte-Carlo (LMC) method is used to obtain  $\alpha_\infty$  from the voxel discretized electrode microstructures. A large number of so-called tracers (typically  $10^6$ ) are placed on pore voxels and perform random walks. During each LMC step, the mean square displacement of all tracers is monitored. Sufficient LMC steps are reached once the temporal derivative of the mean square displacement becomes independent of time, what we typically see after  $2 \times 10^6$  LMC steps. Then, the tortuosity factor is determined by comparing the mean square displacement that is calculated in the pore space geometry to the mean square displacement of unbiased tracers in free space.

### 3.2.3. Electron and oxygen ion migration

As embodied in Eqs. (9) and (10), Ohm's law describes the transport of oxygen ions through the YSZ phase as well as the transport of electrons through the Ni phase, where the effective conductivities  $\sigma_{\text{Ni}}^{\text{eff}}$  and  $\sigma_{\text{YSZ}}^{\text{eff}}$  are required as input parameters. A fully detailed description of our approach for computing the effective conductivities of the Ni and YSZ phases from the voxel discretized microstructures can be found in Ref. [45]. This approach is again based on the Lattice-Monte-Carlo (LMC) method and utilizes percolation information obtained in the cluster identification study.

## 4. Results and discussion

### 4.1. Role of Ni coarsening on microstructural features of SOFC anodes

Parameters of the phase field model are chosen such that they mimic the behavior of real SOFC anodes. First, the parameters of the mobility function are chosen as  $M_{\text{Ni}} = 1.0$ ,  $M^* = 0.01$ ,  $h_1 = 0.01$ ,

$h_2 = 0.005$  and  $h_3 = 0.20$ , which ensures that transport mechanisms controlling Ni phase coarsening is dominated by Ni diffusion along Ni-pore interfaces. Young's equation relates surface and grain boundary energies to the dihedral angle at junctions where grain boundaries meet free surfaces. At SOFC operating temperatures, the ratio of Ni grain boundary to surface energy  $\gamma_{\text{GB}}/\gamma_s = 0.25\text{--}0.5$  [46], which yields dihedral angles ranging between  $150^\circ$  and  $165^\circ$ . Therefore, in the phase field model, we set:  $k = 3.0$ ,  $w = \sqrt{2}$  and  $m_H = 1.0$  and  $A_H = 1.0$ , which yields  $\gamma_{\text{GB}}/\gamma_s \sim 0.4$ . Ni phase grain boundary mobility  $M_{\text{GB}}$  is temperature-dependent and can vary by orders of magnitude depending on the geometrical properties of the grain boundary and impurity content [47,48]. In this work, the kinetic coefficient  $L = 1.0$ , which corresponds to grain boundary mobility  $M_{\text{GB}} \sim 10^{-11} \text{ m}^4 \text{ s}^{-1} \text{ J}^{-1}$  typically found in metals [49,50], is employed. Finally, the model parameters describing Ni–YSZ contact angle were set to  $\xi_1 = 5.0$  and  $\xi_2 = 1.0$ .

To verify that the model incorporates the appropriate interfacial energetics, we carried out simulations of neck growth of two originally spherical Ni particles and wetting properties of a Ni particle deposited on YSZ. The results are shown in Fig. 5(a) and (b), respectively. As can be seen in Fig. 5(a), the contact between two Ni particles at the end of the simulation is characterized by a dihedral angle  $\approx 155^\circ$ . Furthermore, as shown in Fig. 5(b), the observed Ni–YSZ wetting angle is  $\approx 123^\circ$ . Both angles are representative of experimentally observed ones in the Ni–YSZ SOFC anode system.

Having demonstrated that the model properly incorporates interfacial energetics, we start our exploration of the model by examining the virtual SOFC anode systems with various Ni to YSZ particle size ratios, or  $R_{\text{Ni}}/R_{\text{YSZ}}$ . Each virtual SOFC cermet anode is discretized to produce a simulation box of size  $120 \times 120 \times 120$  voxels, where the voxel size is  $\Delta x = \Delta y = \Delta z = 1.0$ . Periodic boundary conditions in all three dimensions are used in the phase field simulations. First, we qualitatively investigate the morphological evolution due to Ni coarsening. For the R2.5 anode system, where  $R_{\text{Ni}} = 0.4R_{\text{YSZ}}$ , panels (a)–(c) of Fig. 6 depict the evolution of Ni phase spatially isolated clusters, where every Ni cluster is assigned a unique color at (dimensionless) coarsening times 0,  $10^3$  and  $10^4$ , respectively. Initially, a single and highly intertwined cluster constitutes most of the Ni phase. As the anode system evolves over time, parts of the Ni skeleton break into smaller clusters, as can be seen in Fig. 6(b) and (c), which eventually leads to loss of percolation degree  $P_D$ . This loss of percolation degree by fragmentation of large clusters into smaller ones will be discussed in more detail later in this section.

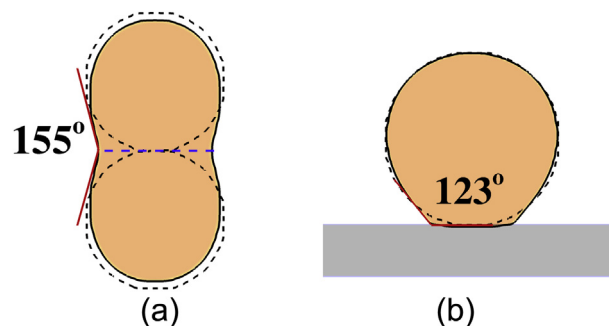


**Fig. 5.** (a) Simulation of the morphological evolution of two Ni grains (orange) where  $\gamma_{\text{GB}}/\gamma_s \sim 0.4$  and the resulting dihedral angle of  $\sim 155^\circ$ . The dashed blue line is drawn to indicate the spatial location of the grain boundary. (b) Simulation of Ni (orange) interaction with a rigid YSZ (gray) substrate and the resulting wetting angle of  $\sim 123^\circ$ . In both panels, dashed and solid black lines represent initial and equilibrium configurations, respectively. (For interpretation of the references to color in this figure legend, the reader is referred to the web version of this article.)



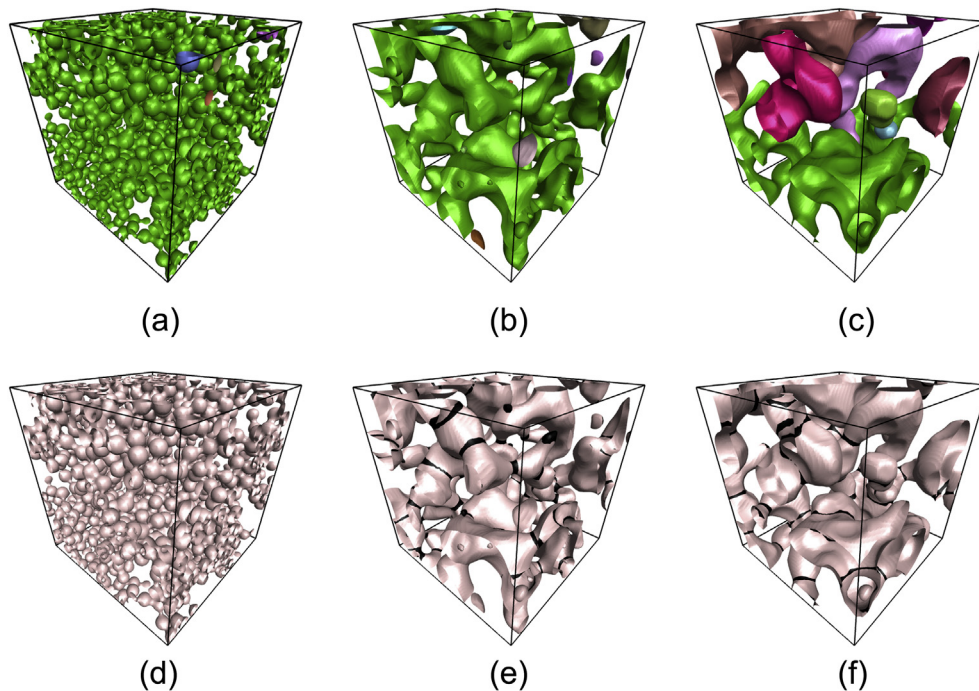


**Fig. 6.** For the R2.5 anode system ( $R_{Ni} = 0.4R_{YSZ}$ ). (a)–(c) Iso-surfaces of spatially isolated Ni clusters with each cluster assigned a unique color at time (a)  $t = 0$  (b)  $t = 10^3$ , and (c)  $t = 10^4$ . (d)–(f) Temporal evolution of the Ni phase grain morphology, with Ni grain boundaries colored in black. (d)  $t = 0$ , (e)  $t = 10^3$ , and (f)  $t = 10^4$ . Note that the static YSZ particles are omitted from the visualizations for clarity.

Next, we examine the temporal evolution of the Ni phase morphology. Panels (d)–(f) of Fig. 6 depicts the temporal evolution of the grain morphology of the Ni phase for the R2.5 anode system. Initially, a collection of small spherical particles constitutes the Ni phase. As the anode system evolves over time, Ni grain growth is observed, where the average size of grains increases and the number of Ni grains shrinks. In addition to Ni coarsening, where the total interfacial energy is minimized, grain growth leads to reduction in the total interfacial energy associated with grain boundaries.

We now turn our attention to several microstructural features affecting the electrochemical performance. We first start by examining the role of microstructure (Ni to YSZ particle size ratio) on the evolution of TPB regions. Within the phase field framework, TPB regions are defined as spatial regions where interfaces of all phase fields meet and overlap. Therefore, the total number of volume elements (voxels), where the Ni, YSZ, and pore phases meet, is regarded as a measure of total TPB, or  $\Lambda_{tot}^*$ . Fig. 7(a) is a plot of  $\Lambda_{tot}^*$

for all systems. It can be clearly seen that for a fixed YSZ particle size, systems with smaller initial Ni particles lead to higher  $\Lambda_{tot}^*$ . A quantity of critical importance when modeling electrochemical reactions is reactive TPB, or  $\Lambda_{react}^*$ , which is defined in this work as the total number of elements, where percolating Ni clusters meet the YSZ and pore phases. Fig. 7(b) is a plot of the temporal evolution of  $\Lambda_{react}^*$ . At late coarsening times, systems with smaller initial Ni particles experience a sharper decrease in  $\Lambda_{react}^*$ . This is due to the loss of percolation of some Ni clusters, as will be shown later in this section.

It is worth noting that the TPB data is expressed in non-dimensional units in order to allow for the investigation of electrochemical performance of porous anodes with a broad range of Ni and YSZ particle size and ratio. The results shown in Fig. 7 can be made dimensional by assigning a value to the characteristic length scale  $d_0$ , which sets Ni and YSZ particle size along with the characteristic time  $\tau$ . For example, assuming  $d_0 = 40$  nm, which corresponds to  $\tau \sim 35$  s, a simulation box of  $(4.8 \mu\text{m})^3$ , and YSZ particle size of  $1 \mu\text{m}$  ( $R_{YSZ} = 0.5 \mu\text{m}$ ), Table 3 lists reactive TPB density for two SOFC anode systems, R1 and R2, at the initial configuration and end of simulation, which corresponds to a (dimensional) coarsening time  $\sim 100$  h. Simulation results for both absolute value and relative change of reactive TPB density in these systems, Table 3, are in good agreement with experimental observations, where a factor of  $\sim 2$  reduction in reactive TPB density was observed [25,26].

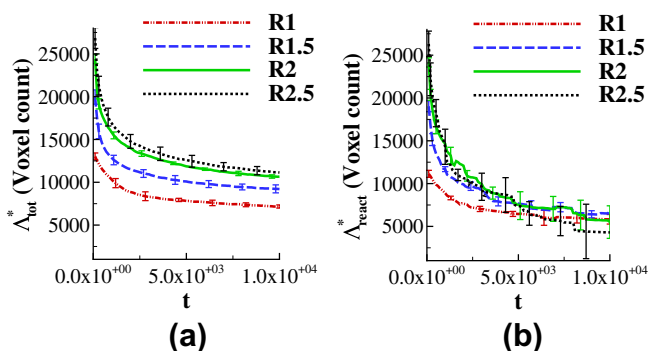


**Fig. 7.** Temporal evolution of (a) total TPB  $\Lambda_{tot}^*$  (b) reactive TPB  $\Lambda_{react}^*$ . In both figures, TPB is measured by the voxel count of elements that are spatially located at Ni–YSZ–pore interfaces.

**Table 3**

Assuming a characteristic length scale  $d_0 = 40$  nm, reactive TPB density for two SOFC anode systems, R1 and R2, with Ni and YSZ particle radii ( $R_{Ni}$ ,  $R_{YSZ}$ ) = (0.5  $\mu\text{m}$ , 0.5  $\mu\text{m}$ ) and (0.25  $\mu\text{m}$ , 0.5  $\mu\text{m}$ ), respectively.

$R_{Ni}$ [ $\mu\text{m}$ ]	$R_{YSZ}$ [ $\mu\text{m}$ ]	TPB [ $\text{mm}^{-3}$ ]		Change [%]
		Initial	After $\sim 100$ h	
0.5	0.5	$5.24 \times 10^{12}$	$3.04 \times 10^{12}$	–42
0.25	0.5	$5.63 \times 10^{13}$	$1.76 \times 10^{13}$	–69



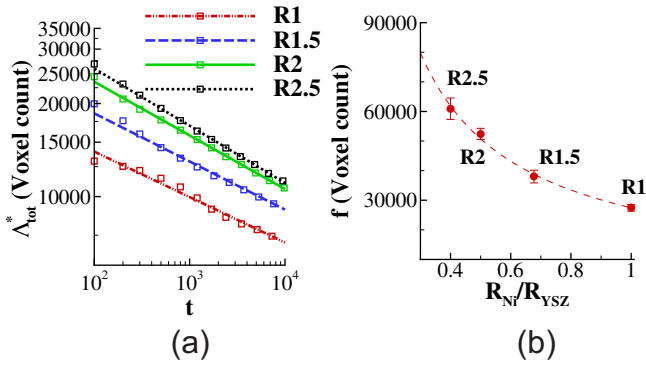


**Fig. 8.** (a) On a log–log scale, total TPB  $\Lambda_{\text{tot}}^*$  vs. coarsening time. (b) The pre-factor  $f = f(R_{\text{Ni}}/R_{\text{YSZ}})$ , where  $\Lambda_{\text{tot}}^*$  is assumed to follow:  $\Lambda_{\text{tot}}^* = f(R_{\text{Ni}}/R_{\text{YSZ}})t^\rho$ . The dashed line is drawn for clarity.

Now, a close examination of Fig. 7(a) reveals a self similar behavior for the temporal evolution of  $\Lambda_{\text{tot}}^*$  during Ni coarsening. Fig. 8(a) is a log–log plot of  $\Lambda_{\text{tot}}^*$  vs. time, where  $\Lambda_{\text{tot}}^*$  is shown to be consistent with a power law of the form

$$\Lambda_{\text{tot}}^* = f \times t^\rho, \quad (12)$$

where the exponent  $\rho = -0.16 \pm 0.02$  and  $f = f(R_{\text{Ni}}/R_{\text{YSZ}})$  is a pre-factor, which encompasses the effects of anode microstructure. Fig. 8(b) in turn demonstrates the dependency of the pre-factor  $f$  on the Ni to YSZ particle size ratio  $R_{\text{Ni}}/R_{\text{YSZ}}$ , where the dashed line is drawn as a guide to the eye.

Next, we examine the evolution of pore space during the microstructural evolution of SOFC anodes. Fig. 9(a) is a plot of the average pore radius  $R_{\text{pore}}$  normalized by the YSZ particle radius  $R_{\text{YSZ}}$ , which is constant (YSZ is a non-evolving phase) and the same in all systems. In all SOFC anode systems,  $R_{\text{pore}}$  increases during the evolution of Ni phase. We also notice that SOFC anode systems having larger initial Ni particles yield larger pores  $R_{\text{pore}}$ . Fig. 9(b) is a plot of the total pore space interfacial area (with both Ni and YSZ)  $A_{\text{pore}}$  normalized by its initial value  $A_{\text{pore}}(t=0)$ . All SOFC anodes experience a continuous decrease in pore interfacial area with systems having smaller initial Ni particles experiencing a larger drop in pore interfacial area. At the end of coarsening simulations, the total decrease in pore interfacial area  $\sim 25\%$ ,  $40\%$ ,  $50\%$  and  $55\%$  for R1 ( $R_{\text{Ni}} = R_{\text{YSZ}}$ ), R1.5 ( $R_{\text{Ni}} = 0.67R_{\text{YSZ}}$ ), R2 ( $R_{\text{Ni}} = 0.5R_{\text{YSZ}}$ ) and R2.5 ( $R_{\text{Ni}} = 0.4R_{\text{YSZ}}$ ) anode systems, respectively. The decrease in total pore interfacial area is primarily due to the temporal evolution of

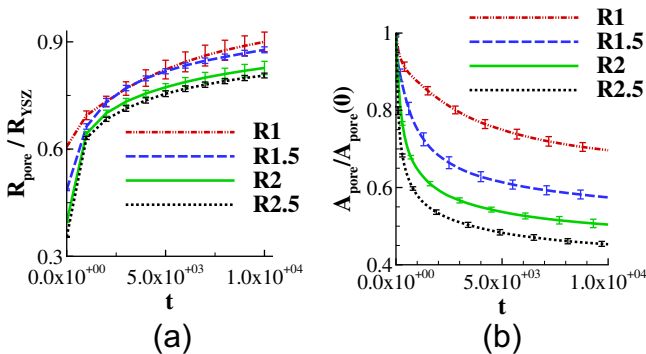


**Fig. 9.** Temporal evolution of the (a) average pore space radius  $R_{\text{pore}}$  normalized by the YSZ particle size  $R_{\text{YSZ}}$  and (b) total pore space interfacial area (with both Ni and YSZ)  $A_{\text{pore}}$  normalized by the initial one  $A_{\text{pore}}(0)$ . Note that the YSZ phase is a non-evolving one and its particles have the same size in all systems.

Ni-pore interfaces. By examining the evolution of pore space, it can be concluded that the pores are growing in size [Fig. 9(a)], and evolving into a more equiaxed shapes, or becoming more round, thus minimizing total interfacial area [Fig. 9(b)]. Our simulation results for the decrease in total pore interfacial area are in good agreement with annealing experiments on Ni–YSZ porous anodes with Ni and YSZ particles of similar size, where a  $\sim 25\%$  decrease in total pore interfacial area was observed [26].

Other effective materials properties are also extracted during the evolution of SOFC anode systems. Fig. 10(a) displays a plot of the pore space tortuosity factor  $\alpha_\infty$ , which affects gas transport mechanisms. Initially, anode systems with smaller initial Ni particles are characterized by larger values for the tortuosity factor. A large  $\alpha_\infty$  value indicates highly twisted paths, which can slow down fuel gas diffusion processes. Ionic/electronic transport mechanisms are influenced by changes in effective conductivities during the microstructural evolution of SOFC anodes. Due to the assumed static, or non-evolving, nature of the YSZ phase, the effective ionic conductivity of the YSZ phase  $\sigma_{\text{YSZ}}^{\text{eff}}$  is constant and approximately the same for all anode systems. Fig. 10(b) in turn quantifies the temporal evolution of the effective electronic conductivity of the Ni phase  $\sigma_{\text{Ni}}^{\text{eff}}$  normalized by the intrinsic Ni phase bulk conductivity  $\sigma_0$ . Initially, systems with smaller Ni particles are characterized by larger  $\sigma_{\text{Ni}}^{\text{eff}}$  values, but as these systems evolve over time, they experience the largest drop in  $\sigma_{\text{Ni}}^{\text{eff}}$ .

Finally, we examine the temporal evolution of Ni phase percolation degree  $P_D$ . Fig. 11(a) is a plot of Ni phase percolation degree as a function of coarsening time. It can be clearly seen, that during Ni coarsening, systems with smaller initial Ni particles experience the largest drop in Ni phase contiguity, i.e., decrease in percolation degree. A close examination of the Ni phase grain morphology reveals that the loss of percolation degree may be associated with the presence of Ni grain boundaries. The two panels in Fig. 11(b) depict a section of a Ni skeleton in the R2.5 anode system, where the top panel (early time) shows a connected Ni cluster. In the bottom panel (late time) of Fig. 11(b), it can be seen that a pinch-off effect along Ni grain boundaries has caused the cluster to lose contiguity. In an experimental study by Nelson et al. [25] on SOFC Ni–YSZ porous anodes under operating conditions with initial Ni and YSZ particles of similar size, they observed trends for the percolation degree that are similar to the ones depicted in Fig. 11(a), where a continuous decrease in Ni phase contiguity was observed.

In more quantitative terms, the temporal evolution of Ni phase percolation degree  $P_D$  can be cast in a functional form as follows:

$$P_D(t) - P_D(0) = G_{\text{ref}}(t/t^*), \quad (13)$$

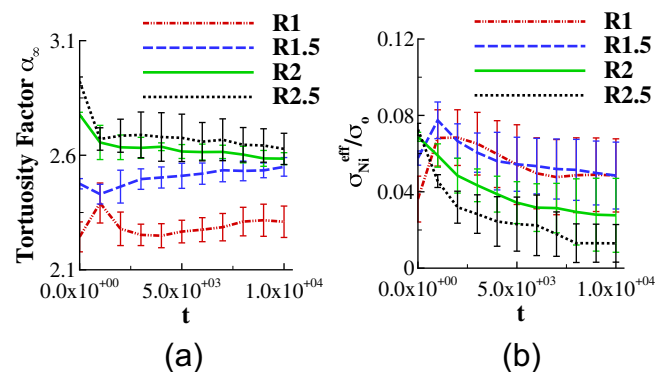


**Fig. 10.** Temporal evolution of (a) pore phase tortuosity factor  $\alpha_\infty$  and (b) Ni phase electron conductivity  $\sigma_{\text{Ni}}^{\text{eff}}$  normalized by the intrinsic Ni bulk conductivity  $\sigma_0$ .

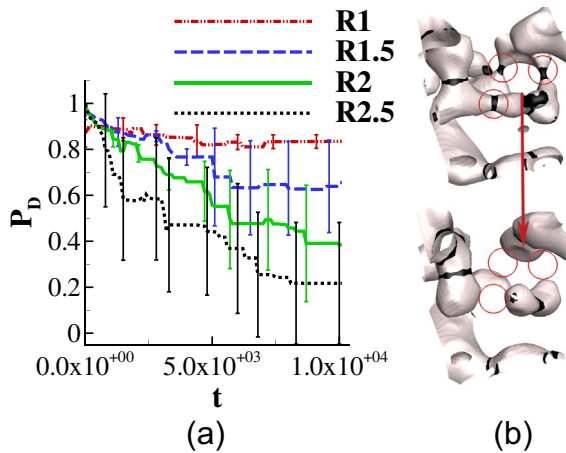


**Fig. 11.** (a) Temporal evolution of Ni phase percolation degree  $P_D$ , which is a measure of percolating Ni clusters that span the simulation box. (b) For the R2.5 anode system, two panels; top (early time) and bottom (late time) showing a section of a Ni skeleton. Circles colored in red show a pinch-off effect at Ni grain boundary regions that leads to morphological instability. Grain boundaries are colored in black. (For interpretation of the references to color in this figure legend, the reader is referred to the web version of this article.)

where  $t^* = t * (R_{Ni}/R_{YSZ})$  denotes a characteristic time scale that controls the loss of percolation degree, while  $G_{ref}$  is a reference functional form for the percolation degree  $P_D$ . The self-similar behavior of Ni phase percolation degree is depicted in Fig. 12(a), while the dependence of  $t^*$  on the ratio  $R_{Ni}/R_{YSZ}$  is in turn depicted in Fig. 12(b). The data can be reasonably well fit with a simple power law function of the form  $t^* \sim (R_{Ni}/R_{YSZ})^\chi$ , where  $\chi \approx 4.1 \pm 2.2$  denotes the effective scaling exponent.

To rationalize this strong dependence of loss of percolation degree on initial Ni particle size, consider the following. If Ni particles in the initial stage are idealized as cylindrical morphologies with “beaded” structures, then the loss of Ni phase percolation degree can be related to the classic Rayleigh instability of inviscid liquid jets [51]. In this case, the cylindrical liquid jet is linearly unstable to perturbations with wavelengths greater than the circumference of the cylinder, and the presence of such perturbations eventually leads to the breaking of the jet into spherical droplets. In the context of solid cylinders, McCallum et al. [52] examined analytically the stability of cylindrical islands on rigid substrates with various wetting angles and demonstrated that the characteristic time for the onset of morphological instability for the

case of surface diffusion  $\tau_s \sim L_d^4/b$ , where  $b$  is a parameter that encompasses various materials properties such as diffusivity and surface tension, and  $L_d$  is a length scale that characterizes the cross-sectional area of the unperturbed cylinder. In addition, we note that grain boundaries also play an important role in the loss of contiguity [cf. Fig. 11(b)]. In particular, during the late stages of the pinch-off process, grain boundary grooving takes place [53]. By extending Mullins’s analysis for a cylindrical bicrystal, it can be shown that the time to pinch-off displays a simple  $R^4$  scaling form, where  $R$  denotes the radius of the unperturbed cylinder. Both of these simple arguments thus suggest a  $t^* \sim (R_{Ni}/R_{YSZ})^4$  scaling form for the characteristic time scale for loss in percolation degree, consistent with our numerical simulations.

#### 4.2. Electrochemical performance

In order to examine the impact of Ni coarsening on the electrochemical performance of SOFCs, we employ the microstructural features and effective material properties that previously have been extracted from evolving anode microstructures as input parameters in our cell level model. So far, no absolute physical dimensions of the simulation box had been assigned in order to keep the results as general as possible, and all dimensions were scaled with respect to the characteristic length scale  $d_0$ . For the electrochemical analysis presented in this section we assign an absolute value to the size of the non-evolving YSZ particles and choose the characteristic length scale,  $d_0$ , accordingly in order to obtain physical measures of the electrochemical performance. For example, a YSZ particle size of  $2 \mu\text{m}$  ( $R_{YSZ} = 1 \mu\text{m}$ ) corresponds to a characteristic length, i.e., a voxel size of  $d_0 = 80 \text{ nm}$ , leading to a  $(9.6 \mu\text{m})^3$  sized simulation box. To account for sample-to-sample variations, effective material properties are averaged over four ensembles for each anode system (R1, R1.5, R2 and R2.5).

Power density vs. current density plots are established for all SOFC cells during the microstructural evolution of SOFC anode systems. Fig. 13(a) shows an exemplary plot of the power density vs. current density for a SOFC cell having an R2.5 anode system, i.e.,  $R_{YSZ} = 1 \mu\text{m}$  and  $R_{Ni}/R_{YSZ} = 0.4$  at the initial time step,  $t = 0$ , and after a coarsening period of  $t = 10^4 \tau$ , corresponding to  $\sim 360 \text{ h}$  in real time for this specific configuration. We define the maximum power density as the peak point in the power density vs. current density curve. A decrease of the maximum achievable power density with coarsening time can be observed in the example, indicating that the changes in the microstructure caused by Ni coarsening lead to a performance loss.

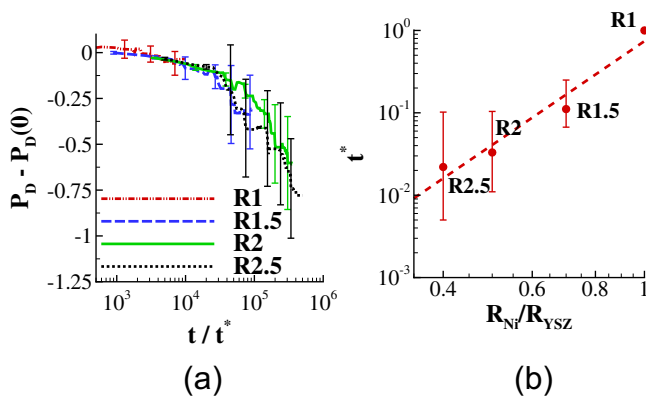


**Fig. 12.** (a) Self similar scaling of Ni phase percolation degree  $P_D$  for all SOFC anode systems. (b) On a log–log scale, characteristic time  $t^* = t * (R_{Ni}/R_{YSZ})$  that sets the morphological instability vs. Ni to YSZ particle size ratio.

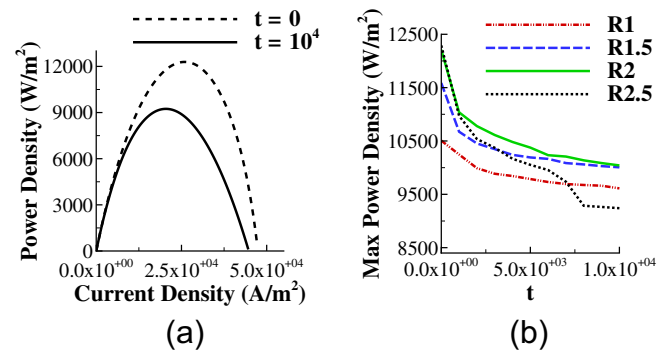


**Fig. 13.** For a YSZ particle size of  $2 \mu\text{m}$  ( $R_{YSZ} = 1 \mu\text{m}$ ). (a) Power density vs. current density plots for a SOFC cell, with the R2.5 anode system ( $R_{Ni}/R_{YSZ} = 0.4$ ), at coarsening times  $t = 0$  (initial) and  $t = 10^4$ . (b) Maximum power density vs. coarsening time for all considered SOFC anode systems. The max. power density is defined as the peak point in the power density vs. current density curve.

To further quantify this effect, we determined the temporal evolution of the maximum achievable power density for all considered anode configurations. Taking  $R_{YSZ} = 1 \mu\text{m}$ , the role of the initial anode microstructure on the evolution of the electrochemical performance during Ni coarsening is quantified in Fig. 13(b). In particular, initial anode microstructures with smaller Ni particles yield higher efficiencies, i.e., values for the maximum power density, which can be explained by their larger amount of available reactive TPB [31]. This is in agreement with recent experimental findings suggesting that SOFCs with anodes having smaller features for the Ni particles yield higher maximum power densities than the ones with anodes having larger Ni particles [54].

Due to the microstructural evolution within the anode, our SOFC cell model predicts a drop in the electrochemical performance during Ni coarsening for microstructures with  $R_{YSZ} = 1 \mu\text{m}$ . This behavior is due to the combined effects of continuous loss of reactive TPB regions, changes of the electronic conductivity in the Ni phase as well as the evolution of pore sizes and pore tortuosity factor. While anodes with initial Ni particles smaller than YSZ ones yield a higher initial maximum power density, such microstructures are also prone to the strongest decline in performance as coarsening takes place. The drop in the maximum power density becomes smoother as the initial sizes of Ni and YSZ particles become comparable. Note that SOFC cells with R2.5 anode systems (i.e.,  $R_{YSZ} = 1 \mu\text{m}$  and  $R_{Ni}/R_{YSZ} = 0.4$ ) experience a sudden drop in the maximum power density at late times  $t \geq 7 \times 10^3 \tau$ . This is strongly correlated with the loss of reactive TPB regions observed in Fig. 7(b), which in turn is associated with the loss of the percolation degree  $P_D$  in the Ni phase as illustrated in Fig. 11(a).

Next, we repeat this approach for a variety of YSZ particle sizes in a range from  $R_{YSZ} = 50 \text{ nm}$  to  $R_{YSZ} = 4 \mu\text{m}$ . Thus, we determine a corresponding characteristic length scale  $d_0$  for each specific  $R_{YSZ}$  value. The purpose of this study is to examine the impact of the absolute size of the YSZ particles in the non-evolving backbone structure on the electrochemical performance during coarsening. As before, for each value of  $R_{YSZ}$ , we consider four cases with different size ratios between Ni and YSZ particles. Each anode microstructure, characterized by its combination of Ni and YSZ particle size and ratio, shows a different initial maximum power density before coarsening takes place. This is caused by the different scaling behavior of the effective material parameters used as input parameters for our cell level model: for example, at a given volume fraction for the anode phases, scaling a given morphology to half of its original size, i.e., reducing the size of the YSZ particles (and also the Ni particles) by 50%, consequently leads to a reduction of the pore size of 50%, while the TPB density is increased by a factor of four [31]. Since we are interested in monitoring relative changes of the performance caused by the microstructural evolution during Ni coarsening, we normalize the values found for the maximum power density in coarsened configurations by their respective initial ones. Contour maps of the normalized power density are generated in order to visualize the results and identify regions of initial YSZ and Ni particle sizes for which the performance is potentially stable against coarsening of the Ni phase.

Fig. 14(a) and (b) shows such maps of the normalized maximum power density at (non-dimensional) simulation times of  $1.0 \times 10^3$  and  $1.0 \times 10^4$ , respectively. [Note that different values of  $R_{YSZ}$  are associated with different values of the characteristic length scale  $d_0$  as mentioned before. According to Eq. (5), this leads in turn to different values of the characteristic time  $\tau$  as  $R_{YSZ}$  is varied.] These maps reveal that the size of the YSZ particles in the non-evolving backbone structure as well as the relative size of the Ni particles have a strong influence on how the performance is impacted by Ni coarsening, as will be discussed next.

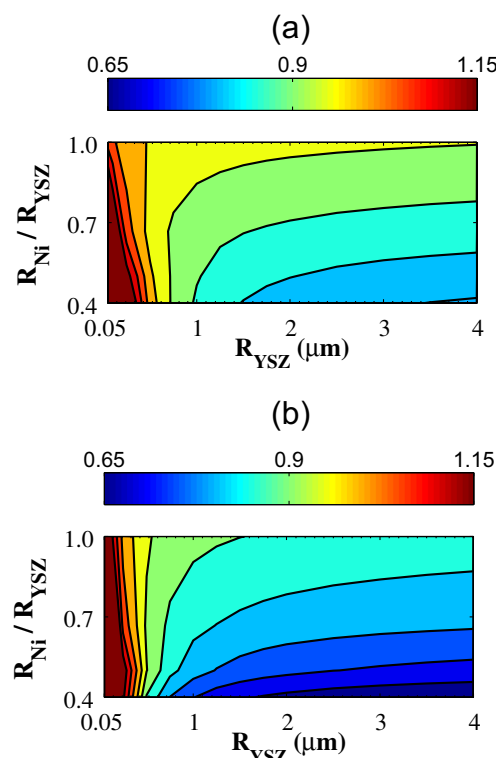


Fig. 14. Maps of the maximum power density normalized by its initial value for various combinations of YSZ particle size and Ni to YSZ particle size ratio ( $R_{Ni}/R_{YSZ}$ ) at coarsening times (a)  $t = 1.0 \times 10^3$  (b)  $t = 1.0 \times 10^4$ .

A close examination of the maps in Fig. 14(a) and (b) reveals that coarsening of the Ni phase causes a degradation of electrochemical performance for YSZ particles of size larger than approximately  $R_{YSZ} > 0.75 \mu\text{m}$ . Furthermore, for systems with smaller YSZ particles ( $R_{YSZ} \leq 0.5 \mu\text{m}$  and  $R_{Ni} < R_{YSZ}$ ) and for the simulation times attained in this study, there exists a time window within which Ni coarsening can even enhance the electrochemical performance. When comparing both maps, i.e., maps of the relative performance change obtained at different simulation time steps, both observed trends become more pronounced at longer simulation times.

We suggest the following explanation for these results. First, we note that porous anode microstructures with a relatively large YSZ particle size, i.e.,  $R_{YSZ} > 0.75 \mu\text{m}$ , also have a sufficiently large average pore size, so that the gas transport through the pore network to and from TPB sites can easily be sustained. However, the amount of active TPB represents the limiting factor for the electrochemical performance of such electrodes. Ni coarsening leads to a reduction of the amount of TPB sites (cf. Fig. 7), so that the overall electrochemical performance degrades as Ni coarsening takes place.

In comparison, anode microstructures with a relatively small YSZ particle size, i.e.,  $R_{YSZ} \leq 0.5 \mu\text{m}$ , and Ni particles of even smaller size, exhibit a sufficient amount of TPB, so that the number of reactive sites does not become rate limiting. However, the small diameters of the porous network become more obstructive for the diffusive gas transport, especially for pore sizes where the Knudsen diffusion becomes comparable to or even dominant over the molecular gas diffusion. We capture this effect in our SOFC cell level model by using the dusty-gas approach that takes both diffusion mechanisms into account. When Ni coarsening takes place in such electrodes, the gas channels in the pore network widen and open up [cf. Fig. 9(a)], which yields improved and alleviated conditions for the diffusive gas transport. While Ni coarsening again leads to a

reduction of TPB, this effect now becomes balanced or even over-compensated by improved gas transport properties due to widening pore sizes. Note that the electronic conductivity of the Ni phase also evolves during coarsening [cf. Fig. 10(b)]. However, as long as a reasonable extent of Ni phase contiguity is maintained, we judge this to have only a minor influence on the performance, since the ionic conductivity of the YSZ phase is orders of magnitude lower than the electronic conductivity of Ni.

In terms of electrochemical efficiency, our model predicts that anodes in the latter regime, i.e., for  $R_{\text{YSZ}} \leq 0.5 \mu\text{m}$  and  $R_{\text{Ni}} < R_{\text{YSZ}}$  are better capable of withstanding the microstructural changes associated with Ni coarsening, provided that the YSZ backbone does not evolve with time and the Ni phase maintains a reasonable level of percolation degree, or contiguity. Therefore, we propose that tuning the initial particle sizes of Ni and YSZ in anode cermets can have a crucial impact on the coarsening behavior and the closely linked temporal evolution of the electrochemical performance during fuel cell operation.

## 5. Conclusions

In summary, an integrated modeling approach was presented in order to quantify the effect of microstructural evolution of Ni–YSZ cermet anodes on the electrochemical performance of SOFCs. A mesoscale phase-field model was developed that captures Ni coarsening in Ni–YSZ cermet anodes, accounts for the polycrystalline nature of Ni, and tracks the evolution of several microstructural features that influence the electrochemical performance. These features were then extracted and used as inputs in a macroscale cell level model that encompasses gas transport, electron and ion conduction processes as well as the electrochemical reactions in order to examine the role of Ni coarsening on electrochemical performance. While the electrochemical model itself is time-independent, its inputs, which represent effective properties, were extracted from the phase field model as Ni–YSZ porous anodes evolved over time. Therefore, the cell level model is capable of capturing the temporal evolution of the electrochemical performance of SOFCs. Initial anode microstructures were idealized as binary mixtures of spherical Ni and YSZ particles and the integrated modeling approach was employed, in a parametric study, to examine the role of initial anode microstructure on the morphological stability of cermet anodes and electrochemical performance of SOFCs.

Our simulation results revealed simple scaling laws for the decrease in overall TPB length and loss in Ni percolation degree, or contiguity. A Ni phase size effect was revealed, such that systems with initially smaller Ni particles maintained higher density of TPBs but lost contiguity faster than the ones with larger Ni particles. Finally, the overall electrochemical performance displayed a non-monotonic time-dependence during coarsening.

For initially coarse microstructures, the interplay between the ceaseless decrease in reactive TPB density and the increase in average pore radius led to degradation in electrochemical efficiency. On the other hand, for initially fine microstructures, these competing factors, i.e., the decrease in TPB density and rapid increase in average pore space radius led to stabilizing the degradation of electrochemical efficiency. This could be an indication that at these length scales, electrochemical performance is dominated by gaseous transport processes through the pore phase.

In broader terms, our approach highlights the importance of the initial anode microstructure on both the morphological stability of Ni phase and electrochemical performance of SOFCs. Several physical phenomena are identified as possible mechanisms that control Ni phase stability and coarsening rates in SOFC porous anodes. Our integrated modeling approach, which is informed by

the local microstructure, can be used as a design tool to: i) Identify combinations of morphological parameters that yield anode systems with optimal characteristics for the microstructural stability and electrochemical performance of SOFCs, ii) utilize the trends and scaling laws for TPB, Ni contiguity and pore radius to predict the performance of SOFCs under extended use, and iii) explore other avenues aiming at stabilizing Ni phase coarsening, such as doping Ni to increase the wettability with the YSZ backbone.

Finally, the role of electrochemical reactions on the evolution of several materials properties that affect Ni phase coarsening dynamics is not accounted for in our approach. For example, Ni phase atomic mobility depends on the local temperature, which is influenced by electrochemical reactions. Further improvement to our modeling approach, which is the subject of a future research exploration, would incorporate the effects of electrochemistry on Ni phase coarsening dynamics in SOFC anodes. In addition, the role of coarsening on the redox stability, alternating oxidizing and reducing conditions, is an important factor in the design of durable SOFC anode microstructures. To this end, we utilized a recently developed model [55] in combination with the coarsening approach presented in this work to examine the role of Ni phase microstructural evolution on the redox stability of SOFC cermet anodes also consisting of binary mixtures of initially spherical Ni and YSZ particles, the results of which are published elsewhere [62].

## Acknowledgments

The authors gratefully acknowledge the financial support by the Energy Frontier Research Center on Science Based Nano-Structure Design and Synthesis of Heterogeneous Functional Materials for Energy Systems (HeteroFoam) funded by the U.S. Department of Energy, Office of Science, Office of Basic Energy Sciences (award DE-SC0001061). We also acknowledge support from the Center for Scientific Computing at the CNSI and MRL: an NSF MRSEC (DMR-1121053) and NSF CNS-0960316.

## References

- [1] D. Chiappini, A.L. Facci, L. Tribioli, S. Ubertini, *J. Fuel Cell Sci. Technol.* 8 (2011) 031015.
- [2] R.J. Gorte, J.M. Vohs, *Curr. Opin. Colloid Interface Sci.* 14 (2009) 236–244.
- [3] E.D. Wachsmann, K.T. Lee, *Science* 334 (2011) 935–939.
- [4] X.-M. Ge, S.-H. Chan, Q.-L. Liu, Q. Sun, *Adv. Energy Mat* 2 (2012) 1156–1181.
- [5] M.C. Williams, J.P. Strakey, W. a. Surdoval, *J. Power Sources* 143 (2005) 191–196.
- [6] A. Stambouli, E. Traversa, *Renew. Sustain. Energy Rev.* 6 (2002) 433–455.
- [7] E. Ryan, W. Xu, X. Sun, M. Khaleel, *J. Power Sources* 210 (2012) 233–242.
- [8] R.M. Ormerod, *Chem. Soc. Rev.* 32 (2003) 17–28.
- [9] W. Zhu, S. Deevi, *Mater. Sci. Eng. A* 362 (2003) 228–239.
- [10] A. Atkinson, S. Barnett, R.J. Gorte, J.T.S. Irvine, a. J. McEvoy, M. Mogensen, S.C. Singhal, J. Vohs, *Nat. Mater.* 3 (2004) 17–27.
- [11] L. Holzer, B. Iwanschitz, T. Hocker, B. Münch, M. Prestat, D. Wiedenmann, U. Vogt, P. Holtappels, J. Sfeir, A. Mai, T. Graule, *J. Power Sources* 196 (2011) 1279–1294.
- [12] D. Sarantaridis, A. Atkinson, *Fuel Cells* 7 (2007) 246–258.
- [13] C.S. Montross, H. Yokokawa, M. Dokiya, *Br. Ceram. Trans.* 101 (2002) 85–93.
- [14] C. Su, R. Ran, W. Wang, Z. Shao, *J. Power Sources* 196 (2011) 1967–1974.
- [15] K. Haga, S. Adachi, Y. Shiratori, K. Itoh, K. Sasaki, *Solid State Ionics* 179 (2008) 1427–1431.
- [16] M. Gong, X. Liu, J. Tremblay, C. Johnson, *J. Power Sources* 168 (2007) 289–298.
- [17] S.P. Jiang, *J. Mater. Sci.* 38 (2003) 3775–3782.
- [18] J.H. Lee, H. Moon, H.W. Lee, J. Kim, J.D. Kim, K.H. Yoon, *Solid State Ionics* 148 (2002) 15–26.
- [19] P.W. Voorhees, *J. Stat. Phys.* 38 (1985) 231–252.
- [20] R.W. Balluffi, S.M. Allen, W.C. Carter, *Kinetics of Materials*, Wiley, 2005.
- [21] D. Simwonis, F. Tietz, D. Stover, *Solid State Ionics* 132 (2000) 241–251.
- [22] P. Tanasini, M. Cannarozzo, P. Costamagna, A. Faes, J. Van Herle, A. Hessler-Wyser, C. Comninellis, *Fuel Cells* 9 (2009) 740–752.
- [23] A. Faes, A. Hessler-Wyser, D. Presvytes, C.G. Vayenas, J. Van Herle, *Fuel Cells* 9 (2009) 841–851.
- [24] L. Holzer, B. Münch, B. Iwanschitz, M. Cantoni, T. Hocker, T. Graule, *J. Power Sources* 196 (2011) 7076–7089.



- [25] G.J. Nelson, K.N. Grew, J.R. Izzo, J.J. Lombardo, W.M. Harris, A. Faes, A. Hessler-Wyser, J. Van Herle, S. Wang, Y.S. Chu, A.V. Virkar, W.K.S. Chiu, *Acta Mater.* 60 (2012) 3491–3500.
- [26] J.S. Cronin, J.R. Wilson, S.A. Barnett, J. Power Sources 196 (2011) 2640–2643.
- [27] R. Vassen, D. Simwonis, D. Stover, *J. Mater. Sci.* 36 (2001) 147–151.
- [28] H.-Y. Chen, H.-C. Yu, J.S. Cronin, J.R. Wilson, S.A. Barnett, K. Thornton, J. Power Sources 196 (2011) 1333–1337.
- [29] Q. Li, L. Liang, K. Gerdes, L.-Q. Chen, *Appl. Phys. Lett.* 101 (2012) 033909.
- [30] J.H. Kim, W.K. Liu, C. Lee, *Comput. Mech.* 44 (2009) 683–703.
- [31] B. Völker, R.M. McMeeking, J. Power Sources 215 (2012) 199–215.
- [32] Y.U. Wang, *Acta Mater.* 54 (2006) 953–961.
- [33] A. Tsoga, A. Naoumidis, P. Nikolopoulos, *Acta Metall.* 44 (1996) 3679–3692.
- [34] J.W. Cahn, J.E. Hilliard, *J. Chem. Phys.* 28 (1958) 258–267.
- [35] K. Maier, H. Mehrer, E. Lessmann, W. Schule, *Phys. Status Solidi (b)* 78 (1976) 689–698.
- [36] H.P. Bonzel, E.E. Latta, *Surf. Sci.* 76 (1978) 275–295.
- [37] M. Akash, J. Mayo, *Mater. Sci.* 35 (2000) 437–442.
- [38] R. Suwanwarangkul, E. Croiset, M.W. Fowler, P.L. Douglas, E. Entchev, M.A. Douglas, J. Power Sources 122 (2003) 9–18.
- [39] F. Zhao, A.V. Virkar, J. Power Sources 141 (2005) 79–95.
- [40] M. Hussain, X. Li, I. Dincer, J. Power Sources 161 (2006) 1012–1022.
- [41] Y. Gan, M. Kamlah, *J. Mech. Phys. Solids* 58 (2010) 129–144.
- [42] Y. Gan, M. Kamlah, J. Reimann, *Fusion Eng. Des.* 85 (2010) 1782–1787.
- [43] J. Hoshen, R. Kopelman, *Phys. Rev. B* 14 (1976) 3438–3445.
- [44] S. Torquato, *Random Heterogeneous Materials: Microstructure and Macroscopic Properties*, Springer-Verlag, New York, 2002.
- [45] B. Völker, R.M. McMeeking, J. Power Sources (2013) submitted for publication.
- [46] E.A. Clark, R. Yeske, H.K. Birnbaum, *Metall. Trans. A* 11A (1980) 1903–1908.
- [47] G. Gottstein, L.S. Shvindlerman, *Grain Boundary Migration in Metals: Thermodynamics, Kinetics, Applications*, second ed., CRC Press, 2010.
- [48] M. Upmanyu, D.J. Srolovitz, L.S. Shvindlerman, G. Gottstein, *Acta Mater.* 47 (1999) 3901–3914.
- [49] H. Zhang, D.J. Srolovitz, J.F. Douglas, J.A. Warren, *Acta Mater.* 55 (2007) 4527–4533.
- [50] M. Taheri, D. Molodov, G. Gottstein, A. Rollett, *Z. Metallkd.* 96 (2005) 1166–1170.
- [51] L. Rayleigh, *Proc. Lond. Math. Soc.* s1–10 (1878) 4–13.
- [52] M.S. McCallum, P.W. Voorhees, M.J. Miksis, S.H. Davis, H. Wong, *J. Appl. Phys.* 79 (1996) 7604–7611.
- [53] W.W. Mullins, *J. Appl. Phys.* 28 (1957) 333–339.
- [54] T. Suzuki, Z. Hasan, Y. Funahashi, T. Yamaguchi, Y. Fujishiro, M. Awano, *Science* 325 (2009) 852–855.
- [55] F. Abdeljawad, G.J. Nelson, W.K.S. Chiu, M. Haataja, *J. Appl. Phys.* 112 (2012) 036102.
- [56] D. Jeon, J. Nam, C. Kim, *J. Electrochem. Soc.* 153 (2006) A406–A417.
- [57] D. Noren, M. Hoffmann, *J. Power Sources* 152 (2005) 175–181.
- [58] P. Chinda, W. Wechsato, S. Chanchaona, P. Brault, *Fuel Cells* 11 (2011) 184–199.
- [59] B. Todd, J. Young, *J. Power Sources* 110 (2002) 186–200.
- [60] D. Chen, W. Bi, W. Kong, Z. Lin, *J. Power Sources* 195 (2010) 6598–6610.
- [61] K. Grew, J. Izzo Jr., W. Chiu, *J. Fuel Cell Sci. Technol.* 8 (2011) 031001.
- [62] F. Abdeljawad, M. Haataja, *J. Appl. Phys.* (2013) in press, <http://dx.doi.org/10.1063/1.4830015>.